Effects of grain size and β fraction on the deformation modes of a Ti-6Al-2Sn-4Zr-2Mo-Si alloy with equiaxed (α + β) microstructures: Slip trace analysis and multiscale simulation of polycrystal plasticity

Irvin Séchepée, Clara Dubray, Vincent Velay, Hiroaki Matsumoto

Effects of grain size and β fraction on the deformation modes of a Ti-6Al-2Sn-4Zr-2Mo-Si alloy with equiaxed (α + β) microstructures: Slip trace analysis and multiscale simulation of polycrystal plasticity

Irvin Séchepée [a], Clara Dubray [b], Vincent Velay [c], Hiroaki Matsumoto [a,*]

[a] Department of Advanced Materials Science, Faculty of Engineering, Kagawa University, 2217-20 Hayashi-cho, Takamatsu, Kagawa 761-0396, Japan
[b] Université de technologie de Compiègne, Rue du Docteur Schweitzer CS 60319, 60203 Compiègne, France
[c] Institut Clément Ader, Université de Toulouse, CNRS, Mines Albi, INSA, ISAE-SUPAERO, Campus Jarlard, 81013 Albi Cedex 09, France

A B S T R A C T

This study investigates the mechanisms behind the great mechanical properties observed at room temperature for a dual-phase Ti-6Al-2Sn-4Zr-2Mo-Si titanium alloy with equiaxed (α + β) microstructures. More precisely, analyzing the material deformation modes and the possible effects of β fraction and grain size was done to better understand such micromechanisms. With this idea in mind, uniaxial tensile deformation tests were performed at room temperature, and the resulting mechanical behaviors were analyzed. It was observed that increasing β fraction would enhance the overall ductility and work hardening while conversely decreasing the material resistance. Additionally, the material strengthening due to grain size effect, quantified by the Hall-Petch parameter, was also found to be dependent on β fraction. Slip trace analysis was conducted to understand the effects of grain size and β fraction on the activation of the basal<a> , prismatic<a> , and pyramidal<c+a> slip systems and their critical resolved shear stress (CRSS) ratios were established. The qualitative study of CRSS ratios revealed that at smaller grain sizes, the basal<a> slip systems were dominant (e.g. basal/prismatic CRSS ratio of 0.86 for d=2.98 μm) whereas the prismatic<a> slip systems were prevalent and more easily activated for coarser grains (e.g. basal/prismatic CRSS ratio of 1.19 for d=4.21 μm). Such CRSS ratios were then used to identify the material parameters of a self-consistent multiscale model employed to reproduce the tensile behaviors. For a more quantitative analysis, the CRSS values were evaluated and correlated to grain sizes with Hall-Petch relations. Clear correlations regarding grain size and β fraction were found for the CRSS of prismatic<a> and pyramidal<c+a> systems. However, special attention was given to the ambiguous results regarding basal<a> slip systems because of the potential manifestation of the compatibility stresses and grain boundary sliding mechanisms due to the higher density of grain boundaries at small grain sizes.

1. Introduction

With the rise of titanium and its alloys in the aerospace, biomedical, and defense industries, the need to understand how such materials behave has been growing consequently. Microstructural features such as grain morphologies, phase constituents, and grain sizes constitute important elements in grasping the mechanical responses of titanium alloys [1–3]. For instance, it is known that controlling the morphology of the microstructure affects its strength and ductility [3,4] such as globular-equiaxed grains would be more ductile but less resistant than well-oriented lamellar grains. Additionally, it has been studied with the Hall-Petch relationship that the mesoscale grain size directly influences the material strength [3,5,6].

This macroscopic relation, however, does not fully explain the strengthening mechanisms which happen at microscales. With the intent of describing the micromechanisms governing plastic deformation in grains, the crystal plasticity theory has been developed and used [7,8]. It is well-established that the deformation of polycrystalline materials is affected by the interaction of individual grains. As such, crystal plasticity seeks to understand the relationship between individual grains and the global mechanical behavior of the material. Self-consistent models are one approach to modeling this relationship [9,10]. They rely on mathematical algorithms to simulate the deformation behavior of individual grains, considering their crystallographic orientation and shape.

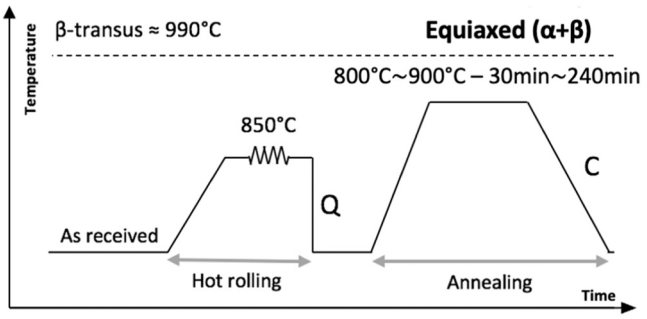

Fig. 1. Thermo-mechanical processing routes of equiaxed (α + β) microstructures.

Then, the overall mechanical response can be obtained by combining the deformation behavior of individual grains and their interactions.

By studying the crystallographic deformation modes (e.g. slip and twinning), we can further understand the plastic deformation in crystalline (metallic) materials. The formation and movement of dislocations, which are linear crystallographic defects or irregularities in the crystal structure, are the main reasons for causing slips. For some titanium alloys such as the Ti-6Al-4V or the Ti-6Al-2Sn-4Zr-2Mo-Si, slips are the most usual deformation mechanisms, especially at room temperature [11,12], and occur on specific planes and directions, respectively called slip planes and slip directions. Slip systems are sets of symmetrically identical slip planes paired with specific slip directions. These characteristics depend on the material and the application temperature [13].

In this study, we focus on a Ti-6Al-2Sn-4Zr-2Mo-Si (Ti-6242S) titanium alloy. Thanks to the extra addition of molybdenum and silicon, this alloy can be used at higher temperatures (≃500 °C), has better creep properties than the popular Ti-6Al-4V alloy (≃350–400 °C) and is used for engine parts. It is also expected the Ti-6242S could be used as a replacement for Ti-64 for lower temperature usage thanks to its better strength (weight saving). Recent research [3] has revealed the Ti-6242S alloy could also exhibit great mechanical properties at room temperature, comparable to those of the Ti-6Al-4V alloy. The Ti-6242S is a near α alloy that can display hexagonal close-packed (HCP) α and/or body-centered cubic (BCC) β crystal structures. HCP crystals essentially deform in five main slip system families which are basal<a> $\{0001\}\langle 11\bar{2}0\rangle$, prismatic<a> $\{10\bar{1}0\}\langle 11\bar{2}0\rangle$, pyramidal<a> $\{10\bar{1}1\}\langle 11\bar{2}0\rangle$, first-order pyramidal<c+a> $\{10\bar{1}1\}\langle 11\bar{2}3\rangle$, and second-order pyramidal<c+a> $\{11\bar{2}2\}\langle 11\bar{2}3\rangle$. However, previous studies [13–15] have shown that basal and prismatic systems exhibited lower critical resolved shear stress (CRSS) to initiate slip, meaning that such systems are more likely to activate compared to pyramidal systems. Yet, prismatic<a> and basal<a> slips can only induce deformation along the <a> direction. Therefore, and because twinning has not been observed in such alloy at room temperature [11,12], only pyramidal<c+a> slips can accommodate strains along the <c> axis during plastic deformation. As for the BCC crystals, $\{110\}\langle 111\rangle$, $\{112\}\langle 111\rangle$, and $\{123\}\langle 111\rangle$ are the main slip system families.

Thanks to crystal plasticity models, it has been possible to fairly evaluate the relationships between microscopic slips and macroscopic deformation behaviors [16,17], texture evolutions [18,19], or plasticity [20] in HCP metals. Contrarily, models predicting deformation in BCC metals are not as accurate as for HCP metals. Indeed, due to the numerous slip systems possible consisting of 12 $\{110\}\langle 111\rangle$, 12 $\{112\}\langle 111\rangle$, and 24 $\{123\}\langle 111\rangle$ systems, the number of parameters to consider and the model complexity are larger. To face such issues, models using pencil glide mechanisms were developed and proved to be equivalent while reducing computational times [21–23].

CRSS values are important material parameters in crystal plasticity computations. However, there is no agreement on standard CRSS values as they are heavily influenced by the material features and the experimental conditions [8,13–16,24,25]. Recently, slip trace analysis has emerged as one method to estimate CRSS ratios by comparing experimental traces observed in SEM with theoretical traces calculated from EBSD orientation maps [13,14,24,25]. H. Li et al. (2013) [24] proposed a complementary analysis using a statistical resampling technique of bootstrapping to minimize the experimental observations and adjust the CRSS ratios.

This paper aims to investigate why the Ti-6242S alloy displayed excellent mechanical properties at room temperature in the author's previous work [3]. Therefore, we opted to study the alloy microstructures and their deformation modes to examine these previous findings. In detail, we focused on checking if grain size and/or β fraction had any effects on the deformation modes of such Ti-6242S alloy with equiaxed (α + β) microstructures. A preliminary study on a macroscale level was made to understand the links between grain size, β fraction, and material strength with an extension of the Hall-Petch equation to dual-phase microstructures. Slip trace analysis was then carried out for several equiaxed microstructure conditions in order to get CRSS ratios and a qualitative understanding of the activation of the slip systems. Using such experimental CRSS ratios, a numerical multiscale model was implemented to reproduce the uniaxial tensile behaviors at room temperature. Fitting the tensile curves by optimizing the numerical parameters allowed us to compute CRSS values. Using Hall-Petch relationships, we investigated the links between grain sizes and CRSS to get a quantitative analysis of the main deformation modes in equiaxed (α + β) microstructures.

2. Experimental procedures

2.1. Heat treatment processes

The titanium alloy Ti-6Al-2Sn-4Zr-2Mo-Si (Ti-6242S) was used in this research. More specifically, its chemical composition (in wt%) consisted of 6.1Al, 2.0Sn, 4.1Zr, 2.0Mo, 0.12Si, 0.1O, 0.02N, and balance Ti. As received plates of 4 mm thickness were hot rolled at 850 °C so that the rolled plates achieved a thickness of 1.3 mm. The equiaxed (α + β) microstructure with globular α grains was looked into for several heat treatment conditions. Indeed, we conducted annealing at both 800 °C and 900 °C for several holding times varying from 30 min to 240 min followed by air cooling (see Fig. 1.).

2.2. Microstructure observations

We used a JEOL JSM-7001F field emission gun scanning electron microscope (FE-SEM) fitted with an electron back-scattering diffraction (EBSD) analyzer equipped with the HKL Channel 5 software in order to observe the microstructures of the different samples. EBSD mapping was done using an acceleration voltage of 15 kV, a beam current of 17 nA, and a step size of 0.15 μm (microstructure average grain sizes range between 2 μm and 5 μm). Concerning the phase parameters, the HCP α was indexed to the 6/mmm Laue group (hexagonal high) with unit cell lengths of a=b= 2.95 Å and c= 4.73 Å. The BCC β phase was indexed to the m3m Laue group (cubic high) with unit cell lengths of a=b=c= 3.19 Å. Grain sizes and phase proportions were estimated with the ImageJ software and using a statistical procedure (mean value of several grain sizes from several SEM micrographs). We considered grains as spherical inclusions (circular in 2D) and computed the average grain size by measuring the surface area S and linking it to an equivalent diameter with $d_{eq} = 2\sqrt{S/\pi}$. Additionally, a dislocation substructure was observed by TEM (JEM-2100F, JEOL, Japan) on thin-foil specimens prepared using an ion-polishing system.

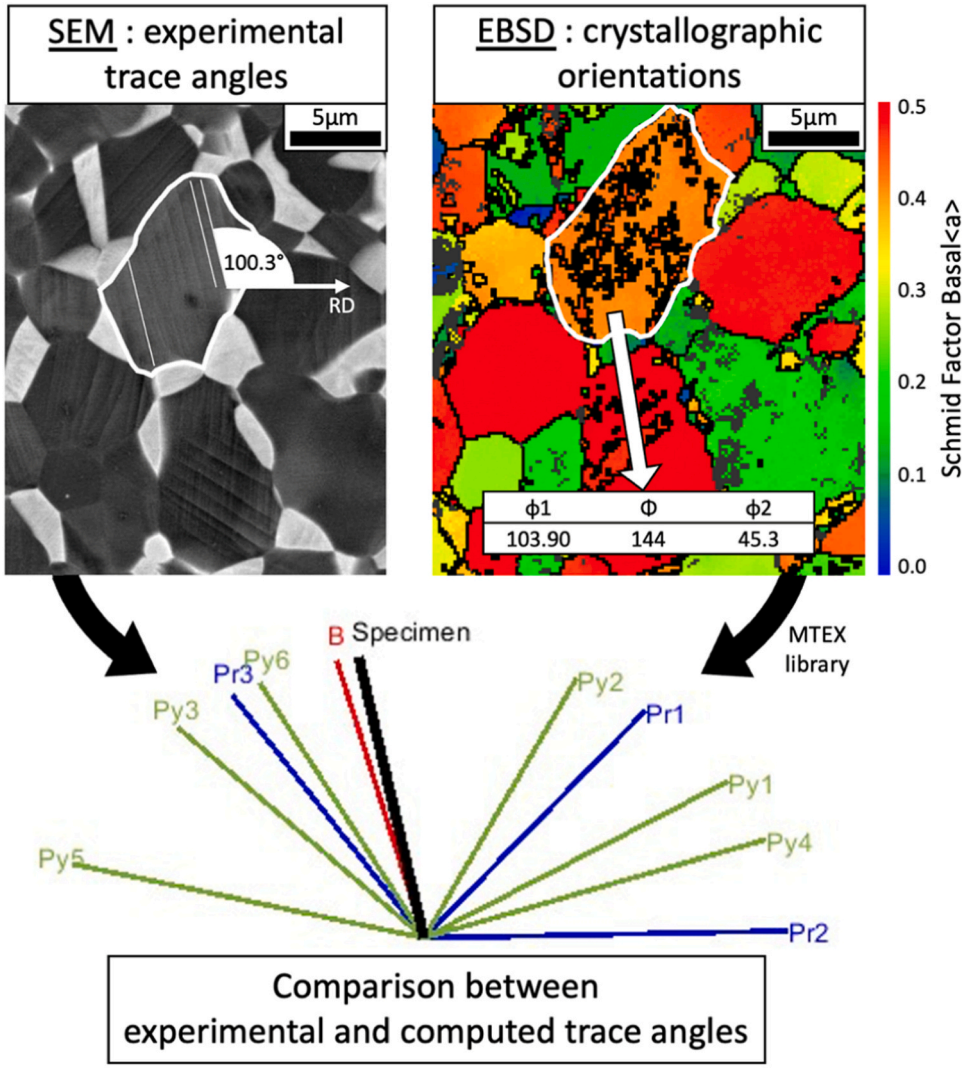

Fig. 2. Methodology for slip trace analysis.

2.3. Tensile tests

Relevant tensile properties such as 0.2% proof stress, ultimate tensile strength (UTS), and elongation to fracture were measured by tensile testing in the rolling direction (tensile and rolling directions are parallel). Regarding the slip trace analysis, tensile testing was interrupted at approximately 5% of strain with the tensile direction of the sample perpendicular (90 °) to the rolling direction so that slip traces could be more heterogeneously activated.

In each case, the tensile specimens had a gauge of 10.5 mm, a width of 2 mm, and a thickness of 1.2 mm. We performed the tensile tests at room temperature, in air atmosphere, and with an initial strain rate of 5×10^{-4} s^{-1}. Because the study is performed at room temperature, the dominant deformation modes consist mainly of basal<a> $\{0001\}\langle 11\bar{2}0\rangle$, prismatic<a> $\{10\bar{1}0\}\langle 11\bar{2}0\rangle$, and first-order pyramidal<c+a> $\{10\bar{1}1\}\langle 11\bar{2}3\rangle$ slip systems [13].

2.4. Slip trace analysis

Slip trace analysis was carried out following the methodology described in [14,24]. In the present study, we only analyzed the grains individually and did not consider slip transfer i.e. the contribution of the neighboring grains. Therefore, the effects of texture are limited. However, we do investigate the effects of grain size which can modify the nature of the grain boundaries and play a role in slip activity. This topic will be discussed later in the results section.

Moreover, slip trace analysis was only performed on the α phase because clear and visible traces could only be observed for such grains. On the contrary, we couldn't investigate clearly the slip traces of the β phase which was left as an accommodating phase. Indeed, the softer BCC β phase allows to accommodate strains in the microstructure and its proportion is believed to influence the deformation modes of the HCP α phase.

Regarding the methodology (portrayed in Fig. 2), we first compared the experimental slips that could be observed inside the grains in the SEM with the theoretical slips of basal<a> , prismatic<a> , and pyramidal<c+a> systems. The theoretical slips were computed thanks to Euler angles obtained by EBSD mapping and a Matlab script using the MTEX toolbox [26]. The selection of the effective slips was then determined thanks to the Schmid factors and by looking at how close the angles of the experimental slips were to the theoretical slips.

Secondly, a statistical method of resampling by bootstrapping inspired by Li. et al. (2013) [24] and adapted in [14] was used to minimize the error between the number of experimental slips observed and the number of potential slips given by EBSD analysis. Such error is defined as:

$$Er = \sqrt{\sum_{ij}(O_{ij} - \frac{c}{c'_j}.E_{ij})} \text{ with } E_{ij} = \frac{P_{ij}.(\frac{l-1}{N_l})^3}{\sum_{ij}P_{ij}.(\frac{l-1}{N_l})^3}.N_o.$$

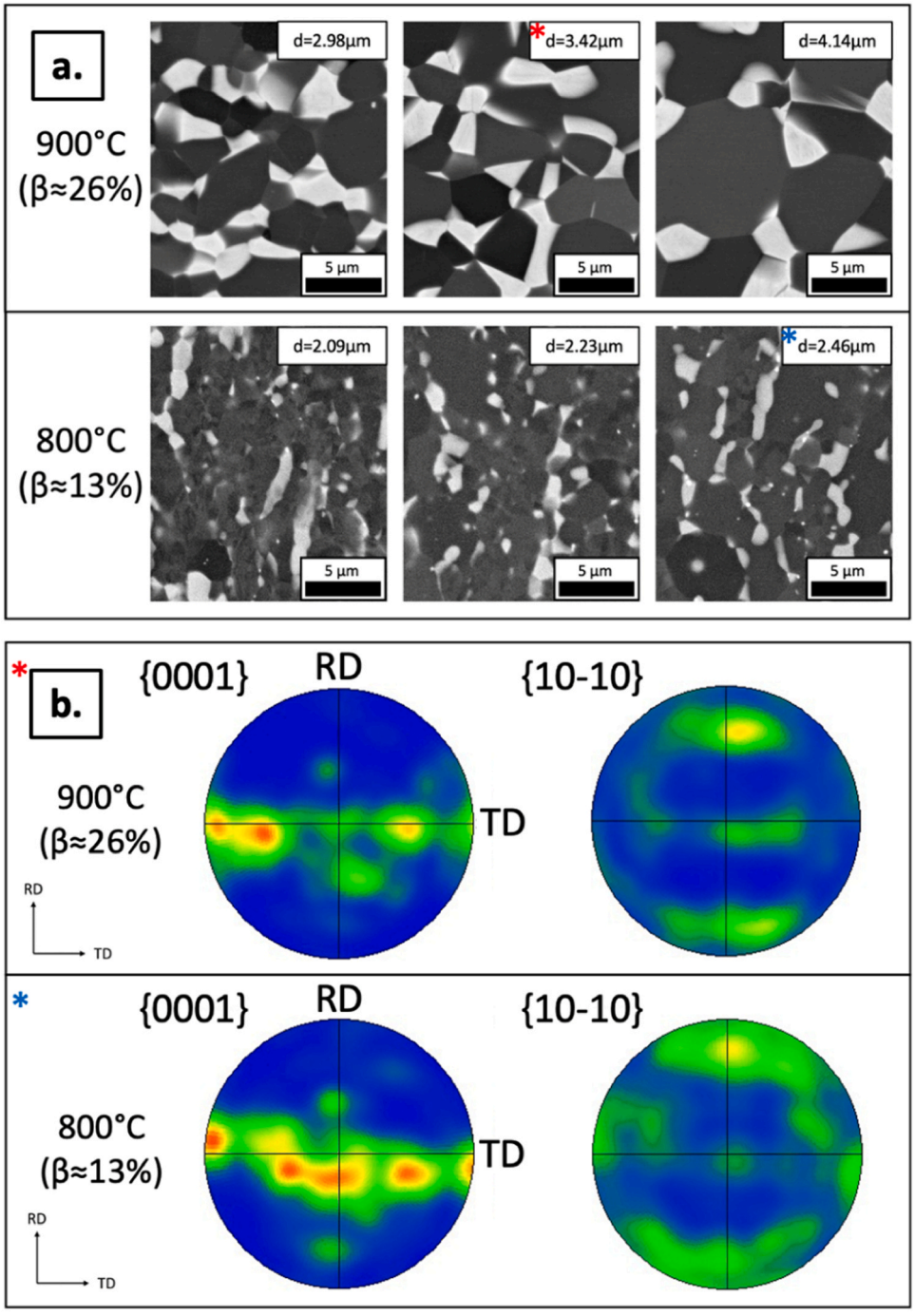

Fig. 3. Typical **a.** SEM images and **b.** EBSD pole figures of equiaxed (α + β) microstructures for the two studied β fractions.

where i is the Schmid factor bin (slip systems were binned regarding their Schmid factor with an increment of 0.05), j is the kind of slip system (basal<a>, prismatic<a>, and pyramidal<c+a>), O_{ij} are the observed (experimental) slip systems, P_{ij} the potential (theoretical) slip systems, E_{ij} the expected (theoretical resampled by a cubic function and taking into account the experimental distribution) slip systems, N_i the total number of bins, N_o the total number of observed slip systems, τ_j^c is the CRSS of slip system j, and c is an unknown constant homogeneous to a constraint (MPa). By minimizing this error, it is possible to assess the CRSS:

$$\frac{\partial E_r}{\partial \tau_j^c} = 0 \Rightarrow \tau_j^c = c.\frac{\sum_i (E_{ij})^2}{\sum_i O_{ij} E_{ij}}$$

and computing CRSS ratios allows to remove the unknown constant c. This optimized correction and the number of experimental observations (above 150 grains) give a more realistic approach to represent the average behavior (local heterogeneities are disregarded) of the material. Thanks to slip trace analysis, the CRSS ratios of basal<a>, prismatic<a>, and pyramidal<c+a> slip systems could be determined for different grain sizes and phase proportions.

2.5. Numerical simulation using multiscale modeling

2.5.1. Mean field approach

The multiscale model used consists of a general formulation of the self-consistent scheme proposed by Berveiller and Zaoui (1979) [9]. The

model is particularly adapted for isotropic elastoplastic intergranular accommodation for plastically flowing polycrystals and is applied here to uniaxial tensile tests. The scale transition is defined as:

$$\sigma_{ij} = \Sigma_{ij} + 2\alpha\mu(1-\beta)\left(E^p_{ij} - \epsilon^p_{ij}\right)$$

where Σ_{ij} is the uniform macroscopic stress, E^p_{ij} is the equivalent macroscopic plastic strain, σ_{ij} and ϵ_{ij} are respectively the uniform stress and uniform plastic strain applied in a specific grain.

The parameters α and β are expressed as functions of the Lame's coefficient μ and the Poisson's ratio ν as:

$$\frac{1}{\alpha} = 1 + \frac{3}{2}\mu\frac{E^p}{\Sigma} \;\&\; \beta = \frac{2(4-5\nu)}{15(1-\nu)}$$

The chosen definition of α is an approximate expression of the initial definition used for smaller computation times and described in [9]. Thanks to this scale transition, it is possible to link the macroscopic fields (Σ_{ij}, E^p_{ij}) with the local fields at the grain scale $(\sigma_{ij}, \epsilon^p_{ij})$.

2.5.2. Local constitutive equations

The Ti-6242S with equiaxed (α + β) microstructure contains HCP α grains and BCC β grains. The local constitutive equations of the Méric-Cailletaud model [27] are defined for each slip system of such grains. Therefore, in this study, we focus on basal<a> $\{0001\}\langle 11\bar{2}0\rangle$, prismatic<a> $\{10\bar{1}0\}\langle 11\bar{2}0\rangle$, and pyramidal<c+a> $\{10\bar{1}1\}\langle 11\bar{2}3\rangle$ slips for the HCP grains and $\{110\}< 111 >$ and $\{112\}< 111 >$ slips for the BCC grains. However, to shorten computation times, the pencil glide model [21–23] was used instead of $\{110\}< 111 >$ and $\{112\}< 111 >$ slips.

In this model, the resolved shear stress τ^s of a slip system (s) is given by the Schmid's law:

$$\tau^s = \overline{\overline{\sigma}}^{g} : \overline{\overline{m}}^{s}$$

where $\overline{\overline{\sigma}}^{g}$ is the stress tensor in a grain (g) and $\overline{\overline{m}}^{s}$ is the orientation tensor of the slip system (s) defined as:

$$\overline{\overline{m}}^{s} = \frac{1}{2}\left(\vec{l}^{s} \otimes \vec{n}^{s} + \vec{n}^{s} \otimes \vec{l}^{s}\right)$$

with $\vec{n}^{s}$ and $\vec{l}^{s}$ being the unit vectors of respectively the slip plane normal and the slip direction.

For each slip system, it is possible to describe the hardening of the material thanks to internal variables like isotropic hardening R^s and kinematic hardening X^s . However, because only monotonic tensile behavior is modeled in this study, hardening parameters can only be calibrated for isotropic hardening [28–30]. Indeed, cyclic loading conditions should be required to clearly distinguish isotropic and kinematic hardenings so that the parameters of both hardening variables can be calibrated. Therefore, kinematic hardening was neglected in this study and the viscoplastic shear rate $\dot{\gamma}^s$ can be written as the Norton type law:

$$\dot{\gamma}^S = \left\langle \frac{\tau^s - R^s}{K} \right\rangle^n \cdot sign\left(\tau^s\right) \text{ with } \langle x\rangle = \max(x, 0)$$

In this equation, n and K are parameters controlling the viscosity. Previous studies have shown there were very little effects of strain rate on the flow stress of such titanium alloys at room temperature [31,32]. Therefore, these viscous parameters were manually calibrated in order to have low viscous effects (i.e. no effect of strain rate) and were set to $n = 10$ and $K = 5$ MPa for each slip system. The isotropic hardening is defined as a non-linear function involving an interaction matrix $\overline{\overline{h}}$ with self and latent hardening:

$$R^s = R^s_0 + Q^s \sum_j h^s_j \left(1 - e^{-b^s v^j}\right) \text{ with } \dot{v}^j = \left|\dot{\gamma}^j\right|.$$

The interaction matrix of the HCP α phase is a symmetric matrix and characterized as:

	B1	B2	B3	P1	P2	P3	Py1	Py2	Py3	Py4	Py5	Py6
–	–	–	–	–	–	–	–	–	–	–	–	–
B1	h_{1B}	h_{2B}	h_{2B}									
B2		h_{1B}	h_{2B}		h_{b-p}				h_{b-py}			
B3			h_{1B}									
–	–	–	–	–	–	–	–	–	–	–	–	–
P1				h_{1P}	h_{2P}	h_{2P}						
P2					h_{1P}	h_{2P}			h_{p-py}			
P3						h_{1P}						
–	–	–	–	–	–	–	–	–	–	–	–	–
Py1							h_{1Py}	h_{2Py}	h_{2Py}	h_{3Py}	h_{2Py}	h_{2Py}
Py2								h_{1Py}	h_{2Py}	h_{2Py}	h_{3Py}	h_{2Py}
Py3									h_{1Py}	h_{2Py}	h_{2Py}	h_{3Py}
Py4										h_{1Py}	h_{2Py}	h_{2Py}
Py5											h_{1Py}	h_{2Py}
Py6												h_{1Py}

Because there is very little information on the interaction parameters of titanium alloys, self-hardening parameters were set to $h_{1s} = 1$, latent parameters between systems of the same family (e.g. basal-basal interactions) were fixed at $h_{2s} = h_{3s} = 1$ and latent parameters between systems from different families were set to $h_{b-p} = h_{b-py} = 1.2$ while interactions between prismatic and pyramidal systems were neglected ($h_{p-py} = 0$) as results from N. Bertin et al. (2014) [20] imply. Nonetheless, it also simplifies a lot the optimization process as there are fewer parameters to optimize.

Finally, the plastic deformation can be calculated for each grain as the result of all slips:

$$\overline{\overline{\dot{\epsilon}}}^{p} = \Sigma_s \dot{\gamma}^s \overline{\overline{m}}^{s}$$

2.5.3. Optimization process and RVE

Apart from the viscous and interaction parameters that were manually set as described in the previous part, only the isotropic hardening parameters of each slip system were identified by optimization process using a genetic algorithm. We took into consideration the CRSS ratios found with slip trace analysis in order to constrain the R_0 (CRSS)

parameters between the different slip systems. Moreover, we chose to put optimization limits so that prismatic<a> CRSS would be located around 300 MPa to be close to the literature [14,33–35]. We also decided to bind the saturation stress parameters Q to R_0 with an equivalent ratio measured on the macroscopic tensile curve using: $Q^s = R_0^s \cdot \frac{UTS - R_{p02}}{UTS}$. The idea was to restrict Q because we observed it had less effect on the simulation results and was quite free as compared to R_0 and the saturation rate b. Finally, we chose to keep identical saturation rates for each slip system in order to keep some consistency when analyzing the different microstructures and to mainly focus on the effect of CRSS.

Concerning the number of grains studied, grain orientations were manually picked up for each grain α present in the EBSD map. Using their Schmid factor, the α grains were then classified into potential categories (basal, prismatic, pyramidal, mix basal-prismatic, mix basal-pyramidal). Finally, we clustered the grains according to their statistical distribution in the EBSD map so that the same relative amount of category was represented in the clusters. Regarding the β grains, we chose to give them random orientations as we believe they are not really textured. Representative volume elements (RVE) of 10, 20, 30, 50, and 80 grains were composed following this clustering method and tested on the simulations. It was found no significant changes were observed between the different RVEs so the one of 30 grains was arbitrarily chosen to keep a safe margin.

3. Results and discussion

3.1. Typical microstructures

We examined equiaxed (α + β) microstructures of a Ti-6242S alloy for various treatment conditions. Heat treating the alloy at temperatures lower than the β transus of 990 °C allowed the co-existence of HCP α and BCC β phases.

Typical SEM micrographs show the microstructures in Fig. 3(a) where the black phase corresponds to α and the white one to β. For a given treatment temperature (800 °C or 900 °C), we observed static grain growth occurring regarding holding times. Indeed, the longer the treatment was, the coarser the α grains would grow. At 900 °C, the breakdown regarding holding times is as follows: 30 min (2.98 μm), 60 min (3.40 μm), 90 min (3.42 μm), 180 min (4.14 μm), and 240 min (4.21 μm). At 800 °C, we measured: 30 min (2.09 μm), 90 min (2.23 μm), and 240 min (2.46 μm).

Static grain growth is a thermal-activated process. Therefore, the grain sizes and their growth rate were fairly different for the two temperatures. However, the most significant change observed between the two temperatures was the phase proportions where microstructures at 800 °C would show around 13% of β for 26% at 900 °C (see Fig. 3(a)). Moreover, we did not notice any effects of the holding times on the phase proportions.

Due to the hot rolling process, the samples we used had specific crystallographic orientations. Typical pole figures for the two temperatures studied are displayed in Fig. 3(b). Thanks to them, we could check that the microstructures had strong basal textures in the transverse direction and that prismatic systems were favorably oriented close to the rolling direction. These observations were relevant because the mechanical properties of our microstructures were evaluated by tensile test with the tensile direction being parallel to the rolling direction. It has been shown that the texture of titanium alloys plays a significant role in the mechanical properties [1,2,36]. Therefore, a multiscale analysis of the grains behavior would highly emphasize the activation of prismatic slip systems during such tensile testing.

3.2. Tensile behaviors

Thanks to uniaxial tensile testing, we assessed the flow behaviors of our samples. Fig. 4(a) highlights the typical stress-strain curves we analyzed. We noticed β fraction was connected to the increase of ductility and work hardening ability of the equiaxed (α + β) microstructures as previous work also suggested [3,37]. In (α + β) titanium alloys, β phase is recognized to be more ductile than α phase due to the greater number of slip systems that can be activated in BCC crystals (β) rather than in HCP crystals (α). Indeed, the multiple possible slips among the 12 $\{110\}\langle 111\rangle$, 12 $\{112\}\langle 111\rangle$, and 24 $\{123\}\langle 111\rangle$ systems (total of 48) of BCC crystals grant better deformation properties than the restricted number of 3 basal<a> $\{0001\}\langle 11\bar{2}0\rangle$, 3 prismatic<a> $\{10\bar{1}0\}\langle 11\bar{2}0\rangle$, 6 pyramidal<a> $\{10\bar{1}1\}\langle 11\bar{2}0\rangle$, 12 first-order pyramidal<c+a> $\{10\bar{1}1\}\langle 11\bar{2}3\rangle$, and 6 second-order pyramidal<c+a> $\{11\bar{2}2\}\langle 11\bar{2}3\rangle$ slip systems (30 in total) in HCP crystals. Therefore, the higher proportion of BCC β (=26%) in the 900 °C samples is one first factor to explain its better ductility.

In greater detail, we believe the annealing temperature is at the origin of the ductility and work hardening improvement. First, many dislocations were introduced in the material by forging (hot-rolling) process, resulting in greater strength but lower ductility as it can be seen in the as-rolled tensile curve in Fig. 4(a). The annealing treatment led to the annihilation of dislocations which is a mechanism that increases the ductility. The higher temperature of 900 °C allows to annihilate more dislocations and could be another factor for its better ductility compared to 800 °C. While some dislocations have been annihilated, most of the remaining ones concentrate at grain boundaries. For confirmation purposes, we measured local misorientations using the Kernel Average Misorientation (KAM) measures and by combining several EBSD maps (3 locations for each treatment condition). At 800 °C, average KAM values of 1.09° and 0.97° were respectively found for holding times of 30 mins and 90 mins while the average KAM value went down to 0.66° for 240 mins. At 900 °C, the average KAM values were found constant (from 0.69° for 30 mins to 0.72° for 240 mins). Therefore, we indeed measured full dislocation annihilation at 900 °C whereas some dislocations still remained for short holding times at 800 °C.

Previous researches [38–40] have shown that α-β interfaces would induce more piled-up dislocations at boundaries and result in an increase of both the ductility and the work hardening. β fraction being higher at 900 °C (β = 26%) than at 800 °C (β = 13%), the better work hardening ability and ductility of the 900 °C samples could also be explained thanks to this greater density of α-β interfaces. On the other hand, we noticed the material strength, especially its proof stress is influenced by both β fraction and grain size. Fig. 4(b) relates grain size to proof strength through a Hall-Petch relation and shows different global Hall-Petch constants regarding β fraction. Z. Fan et al. (1993) [6] proposed an extension of the Hall-Petch relation to dual-phase alloys in which the global Hall-Petch constant can be written as functions of α-α, β-β, and α-β boundary contributions:

$$k_y^c = k_y^\alpha f_{\alpha c} + k_y^\beta f_{\beta c} + k_y^{\alpha\beta} F_s$$

with $k_y^c, k_y^\alpha, k_y^\beta$, and $k_y^{\alpha\beta}$ being respectively the global, α, β, and α-β (boundary) Hall-Petch constants, F_s the degree of separation of an α-β mixture (fraction of α-β boundaries). $f_{\alpha c}$ and $f_{\beta c}$ are the continuous volume fractions defined as functions of f_α and f_β volume fractions of α and β phases:

$$F_s = \frac{f_\alpha f_\beta (d_\alpha + d_\beta)}{f_\alpha d_\beta + f_\beta d_\alpha},\ f_{\alpha c} = \frac{f_\alpha^2 d_\beta}{f_\alpha d_\beta + f_\beta d_\alpha},\ f_{\beta c} = \frac{f_\beta^2 d_\alpha}{f_\alpha d_\beta + f_\beta d_\alpha}$$

knowing d_α and d_β, the grain sizes of α and β fraction respectively. Considering this, we can understand that decreasing β from 26% to 13% would imply k_y^α, the Hall-Petch constant of the α phase, is given more importance in characterizing the global Hall-Petch constant k_y^c because there are less β and α-β boundaries. α phase being harder than β phase, it can explain why we observe such differences in the global Hall-Petch constants we measured experimentally and why strength was more sensitive to grain size at lower β proportions.

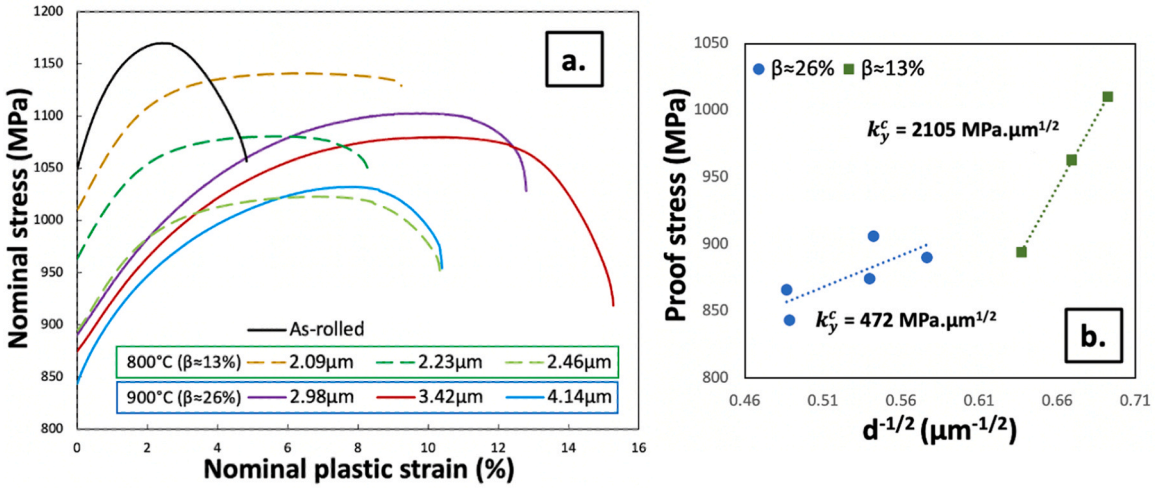

Fig. 4. **a.** Typical tensile stress-strain curves of equiaxed (α + β) microstructures **b.** Macroscopic Hall-Petch relations.

Table 1
Microstructural, topological, and Hall-Petch parameters used/computed with the extended Hall-Petch equation.

Heating temperature	d_α (µm)	d_β (µm)	k_y^c (MPa. µm$^{1/2}$)	f_α (-)	f_β (-)	$f_{\alpha c}$ (-)	$f_{\beta c}$ (-)	F_s (-)	k_y^α (MPa. µm$^{1/2}$)	k_y^β (MPa. µm$^{1/2}$)	$k_y^{\alpha\beta}$ (MPa. µm$^{1/2}$)
900 °C	4	1		0.76	0.24	0.31	0.15	0.54			
800 °C	4	1		0.87	0.13	0.54	0.05	0.41			
900 °C	4.14	2.42	472	0.76	0.24	0.46	0.10	0.44	4524	-123	-3630
800 °C	2.46	0.66	2105	0.87	0.13	0.69	0.03	0.28			

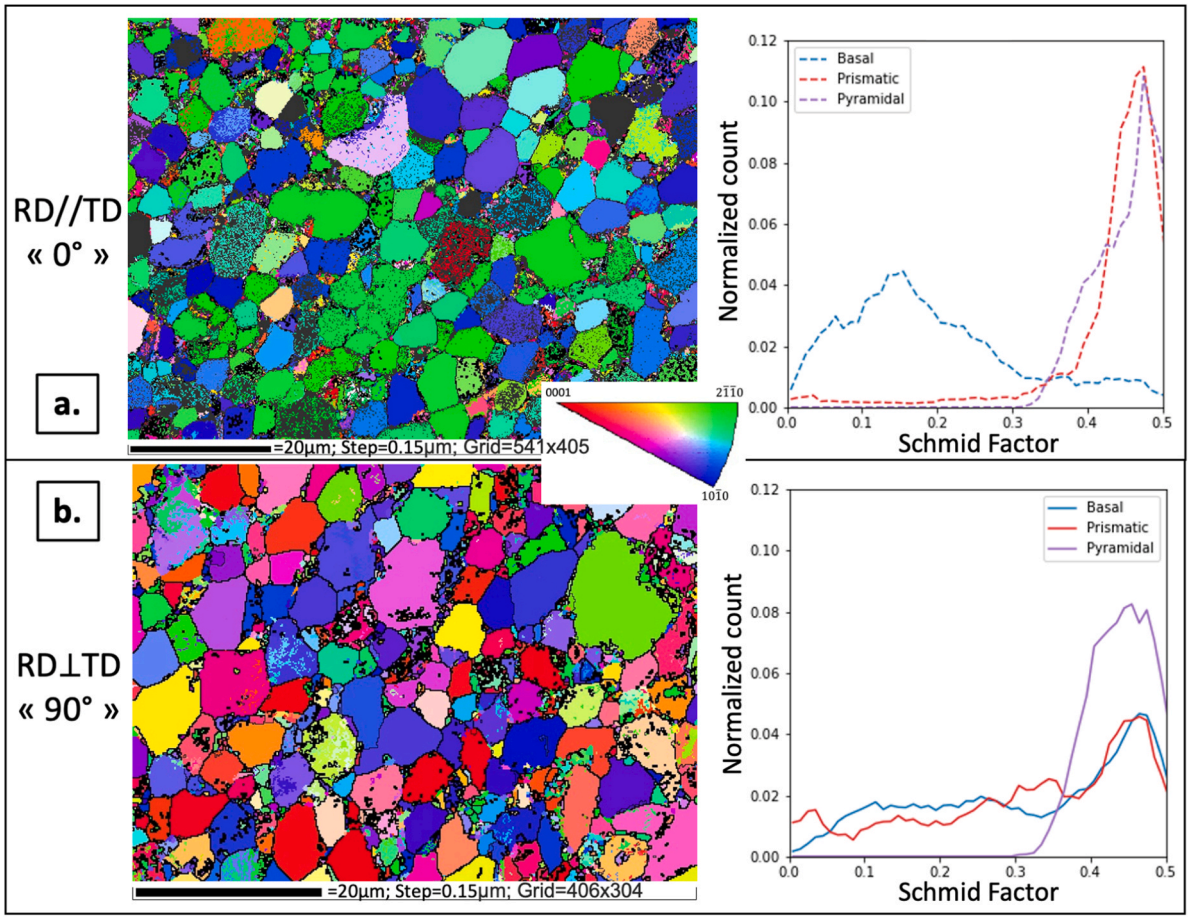

Fig. 5. Typical EBSD IPF maps regarding tensile direction of equiaxed (α + β) microstructures with the rolling direction **a.** parallel to the tensile direction and **b.** perpendicular to the tensile direction.

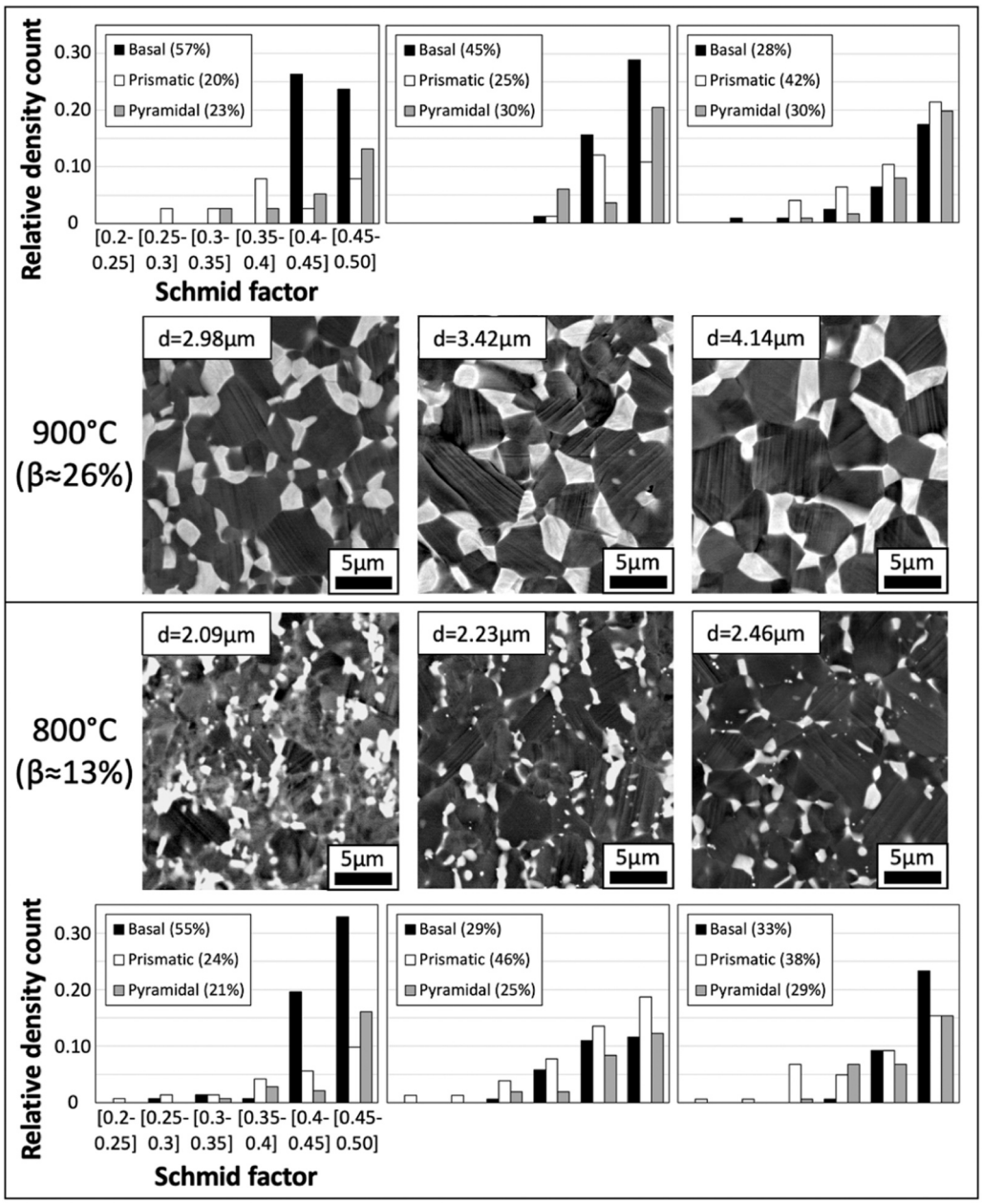

Fig. 6. Typical SEM micrographs with slipped grains and the respective repartitions of the activated slip systems.

To picture the relative importances given to α-α, β-β and α-β boundaries, we computed $f_{\alpha c}$, $f_{\beta c}$, and F_s for a hypothetical scenario and for our experimental data (Table 1). The hypothetical scenario consists of α and β grain sizes that don't change with β fraction (respectively 4 µm and 1 µm). Therefore, this scenario only emphasizes the effect of phase proportions. As mentioned earlier, k_y^{α} is indeed given more importance when decreasing β fraction with $f_{\alpha c}$ (proportion of α-α interfaces) increasing from 0.31 to 0.54 while k_y^{β} and $k_y^{\alpha\beta}$ importances decrease with $f_{\beta c}$ and F_s going down from 0.15 to 0.05 and 0.54 to 0.41 respectively.

The same observation can be made when we consider our set of experimental data where both grain sizes and phase proportions are taken into account. $f_{\alpha c}$ also increases with greater values (0.46 to 0.69) while $f_{\beta c}$ and F_s values are lower. These results highlight the importance given to α-α boundaries as compared to β-β and α-β boundaries in the material strengthening due to grain size effect (k_y^c). Indeed, the Hall-Petch constant denotes the contribution of grain boundaries to the material yielding or, in other words, the resistance of grain boundaries against the movement of dislocations. Here, we can understand the stronger k_y^c at β = 13% comes from the higher density of α-α interfaces that are more resistant to dislocations movement (i.e. slip propagation) than β-β and α-β interfaces (i.e. $k_y^{\alpha} > k_y^{\beta}$ and $k_y^{\alpha} > k_y^{\alpha\beta}$).

The Hall-Petch parameter can be related to grain boundaries or even dislocations and many models have emerged. Among the dislocations pile-up-based models which consider that stresses generated by dislocation pile-ups would activate Frank-read source mechanisms in adjacent grains, R.W. Armstrong et al. (1962) [41] proposed an expression that considers the effect of crystal structure through the Taylor factor:

$$k = m^2 \tau_c \sqrt{l}$$

where τ_c is the CRSS of a deformation mode, m the Taylor orientation factor, and l the distance from the grain boundary. Alternatively, J.C. Li (1963) [42] proposed a model based on grain boundary sources where

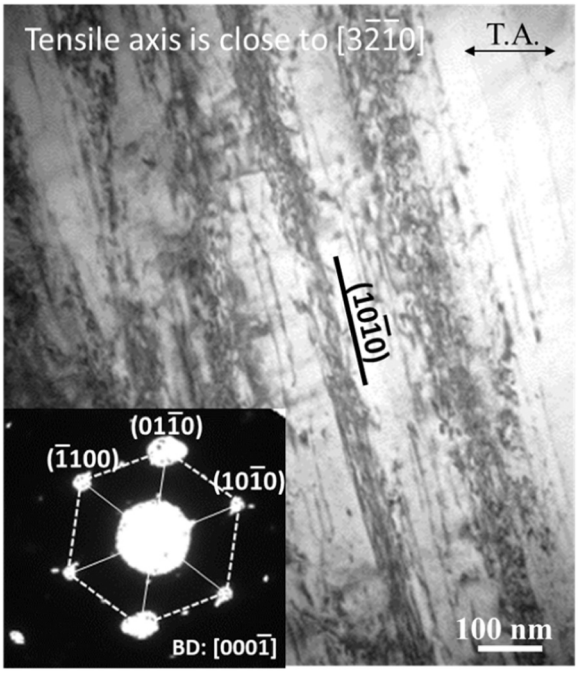

Fig. 7. TEM bright field image and selected area diffraction pattern (beam direction corresponds to ⟨000$\bar{1}$⟩) taken from an α grain in a deformed specimen (d=3.40 μm) with a plastic strain of 12%.

Table 2
CRSS ratio results and comparison with literature.

Alloy used	Basal<a>	Pyramidal<c+a>	Reference
Ti-6242S	**0.82 - 1.2**	**4.08 - 5.78**	**Present study**
Ti-6242S	1.06	1.80	[33]
Ti-6Al-4V	1 - 1.5	3.0 - 3.5	[19]
Ti-6Al-4V	1.33 - 1.41	2.72 - 3.41	[14]
Ti-6Al-4V	0.93 - 1.3	1.1 - 1.6	[38]
Ti-6Al-4V	1.43	4.23	[39]
Ti-6Al-4V	0.93	1.80	[34]
Ti-6Al-4V	1.13	1.61	[40]
Ti-6Al-4V	1.14	1.59	[16]
Ti-6Al	1.01	2.64	[35]
Ti-6Al	0.95	3.85	[17]

dislocations are generated from grain boundaries at yielding and strengthen the material through the Taylor equation:

$$k = \alpha G b\sqrt{3s}$$

with α a material-dependent constant, G the shear modulus, b the Burger's vector, and s the line length of dislocation emitted per unit area of grain boundary. M.F. Ashby (1970) [43] proposed another type of model related to geometrically necessary dislocations (GNDs) and stated that compatible deformation of individual grains in a polycrystal required the introduction of GNDs which affect strength through a Taylor equation:

$$k = \alpha G b\sqrt{\frac{b\varepsilon}{4}} \quad with \quad \frac{b\varepsilon}{4d} = \rho_{GND} + \rho_{SS}$$

where α, G, and b are the same as above, ε is the plastic strain, ρ_{GND} and ρ_{SS} the respective GND and statistically stored dislocation densities. Other researchers, such as J. Luo and Z. Wang (2007) [44] have interestingly suggested the material strengthening effect due to grain boundary was mainly the result of the grain boundary energy density:

$$k = \beta G\sqrt{2a_0\gamma}$$

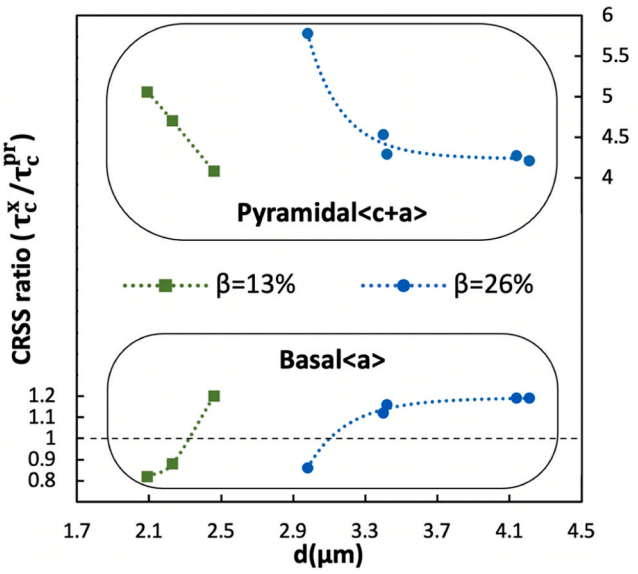

Fig. 8. Evolution of the CRSS ratios for basal<a> and pyramidal<c+a> slip systems.

In this equation, β is a material-independent constant used for dimension consistency, G denotes the shear modulus, a_0 the lattice parameter, and γ the grain boundary surface energy. By seeing the multitude of models available to define the Hall-Petch constant, we can understand it is quite difficult to produce consistent results as they always depend on material constants. However, we can figure out whether the dislocations (pile-up dislocations at grain boundaries and/or GNDs) and/or the grain boundaries themselves play a big role in this strengthening thanks to grain size effect.

Thanks to the extended equation proposed by Z. Fan et al. (1993) [6] detailed earlier, we tried to compute the different k_y from our experimental data. The starting point of the calculation is a strong hypothesis of $k_y^i(\beta = 26\%) = k_y^i(\beta = 13\%)$ for $i = \alpha, \beta, \alpha\beta$. This hypothesis means that the mesoscopic Hall-Petch parameters are independent of β fraction. Thanks to that, we could obtain the system of three variables for two equations:

$$\begin{cases} 0.46k_y^{\alpha} + 0.10k_y^{\beta} + 0.44k_y^{\alpha\beta} = 472 (1) \\ 0.69k_y^{\alpha} + 0.03k_y^{\beta} + 0.28k_y^{\alpha\beta} = 2105 (2) \end{cases}$$

Using elementary operations, we can remove the k_y^{β} term in the first line (1) using the second line (2) with (1') ← (1)− 0.10/0.03(2). On the other hand, we can neglect the contribution of k_y^{β} in (2) thanks to $f_{\beta c} << F_s < f_{\alpha c}$ (0.03<<0.28 <0.69). With these operations, we now have two variables remaining for two equations:

$$\begin{cases} 1.84k_y^{\alpha} + 0.49k_y^{\alpha\beta} = 6545 (1') \\ 0.69k_y^{\alpha} + 0.28k_y^{\alpha\beta} = 2105 (2') \end{cases}$$

We can finally solve the system and compute k_y^{α} and $k_y^{\alpha\beta}$, then inject them into (1) to calculate k_y^{β}. The values are compiled in Table 1. It appears the results are surprisingly peculiar and inconsistent with the experimental values found in [6,45], especially for the negative $k_y^{\beta} = -123$ MPa.μm$^{1/2}$ and highly negative $k_y^{\alpha\beta} = -3630$ MPa.μm$^{1/2}$. Such inverse Hall-Petch results would imply that β-β and α-β interfaces soften the material when decreasing grain size with α-β interfaces being very sensitive to grain size. It suggests that β boundaries assist the movement of dislocations instead of simply opposing it with moderate resistance as compared to α boundaries. Concerning these results, we

Table 3
CRSS values (R0) and other isotropic hardening parameters used in modeling the samples at β = 26%.

	Basal<a> {0001}⟨11$\bar{2}$0⟩			Prismatic<a> {10$\bar{1}$0}⟨11$\bar{2}$0⟩			Pyramidal<c+a> {10$\bar{1}$1}⟨11$\bar{2}$3⟩			Pencil		
β = 26%	R_0	Q	b	R_0	Q	b	R_0	Q	b	R_0	Q	b
d= 2.98 μm	295.2	55.2	0.1	343.3	64.2	0.1	1984.3	371.0	0.1	216.0	40.4	0.1
d= 3.40 μm	329.4	61.6	0.1	284.0	53.1	0.1	1218.4	227.8	0.1	216.0	40.4	0.1
d= 3.42 μm	336.0	62.8	0.1	300.	56.1	0.1	1359.0	254.1	0.1	216.0	40.4	0.1
d= 4.14 μm	311.8	58.3	0.1	262.0	49.0	0.1	1118.7	209.2	0.1	216.0	40.4	0.1
d= 4.21 μm	329.9	61.7	0.1	277.2	51.8	0.1	1167.0	218.2	0.1	216.0	40.4	0.1

Table 4
CRSS values and other isotropic hardening parameters used in modeling the samples at β = 13%.

	Basal<a> {0001}⟨11$\bar{2}$0⟩			Prismatic<a> {10$\bar{1}$0}⟨11$\bar{2}$0⟩			Pyramidal<c+a> {10$\bar{1}$1}⟨11$\bar{2}$3⟩			Pencil		
β = 13%	R_0	Q	b	R_0	Q	b	R_0	Q	b	R_0	Q	b
d= 2.09 μm	365.7	42.2	4.0	446.0	51.7	4.0	2256.8	261.8	4.0	216.0	25.1	4.0
d= 2.23 μm	358.2	41.5	4.0	407.0	47.2	4.0	1912.9	221.9	4.0	216.0	25.1	4.0
d= 2.46 μm	381.6	44.3	6.0	318.0	36.9	6.0	1297.4	150.5	6.0	216.0	25.1	6.0

can think by contradiction and state that our initial hypothesis might be false, meaning that k_y^i should not be unrelated to β fraction. Therefore, we concluded that both the macroscopic k_y^c and the mesoscopic k_y^α, k_y^β, and $k_y^{\alpha\beta}$ were indeed dependent on β fraction.

3.3. Slip trace analysis

In this study and as a first approach, we decided to measure and use CRSS ratios unrelated to crystallographic texture even though we model tensile behavior for hot-rolled equiaxed samples. Indeed, we would like to focus on the effect of texture on slip system activity in a later study.

As mentioned before, the microstructures have a strong prismatic texture alongside the rolling direction. Hence, our EBSD results indicate there is an uneven activation of prismatic systems when exposed to a deformation parallel to such direction. EBSD inverse pole figure (IPF) maps regarding tensile direction are displayed in Fig. 5.

For samples with their rolling direction parallel to the tensile direction (Fig. 5(a)), the grains are indeed favorably oriented for prismatic systems to slip. The distribution of the Schmid factors also supports this observation as prismatic Schmid factors are greatly clustered in the [0.4;0.5] interval, denoting a very high probability of slipping. In contrast, basal Schmid factors are much more dispersed around the 0.15 value and imply a little probability for basal systems to be activated. However, for samples with their rolling direction perpendicular to the tensile directions (Fig. 5(b)), both the IPF map and the Schmid factor distribution show a more balanced distribution of the crystallographic orientations for heterogeneous activations of prismatic and basal slip systems.

According to these observations, we performed slip trace analysis for samples with their rolling direction perpendicular to the tensile directions so that we could get closer to texture-independent CRSS ratios and to literature results [14,16,17,33–35,46–48].

Typical SEM micrographs with slipped grains are presented in Fig. 6. We identified slip traces in an average value of 138 grains for the 900 °C (β = 26%) samples and 79 grains for the 800 °C (β = 13%) ones. We also displayed the distributions of the experimentally observed activated slip systems regarding their Schmid factors. It is worth noticing that basal<a> slip systems were dominantly activated at small grain sizes (more than 50%) for 20–25% of prismatic<a> systems. Contrarily, prismatic<a> slip systems became the dominant deformation modes at coarser grain sizes (around 40%) while basal<a> systems activation was diminished to about 30%. On the other hand, pyramidal<c+a> slip systems were relatively found in the same proportions.

In order to characterize the dislocations substructure in this alloy, Fig. 7 displays a typical one in the tensile deformed specimen (d=3.40 μm) observed by TEM. The tensile axis for the observed α grain is close to the orientation of ⟨3$\bar{2}$1$\bar{0}$⟩. Correspondingly, this grain has a high Schmid factor for prismatic<a> slip. This substructure displays straight-type dislocations that are distributed less uniformly and as planar arrays, that is, there are no apparent cross-slipping traces nor multiple slipping. Additionally, it can be observed that planar dislocation bands are glided on a prismatic plane {10$\bar{1}$0}, according to the selected area diffraction pattern taken in this grain. These planar dislocation arrays result in the slip lines (bands) observed clearly in the slipped grains taken from SEM as shown in Fig. 6. Regarding the planar configuration of dislocations observed in the Ti-6242S alloy, a high amount of Al content should cause it. According to previous works, it is well recognized that increasing the Al content alters the slipping configuration in the α phase [49]. Such alternation initiates at Al contents of 2 wt% where <a> type dislocations are seen to become straight and of screw character. At higher Al contents the arrangement of these straight screw dislocations becomes less uniform and the dislocations are eventually confined to very planar arrays at ~ 6 wt%Al [49]. The planarity of the slip is caused by short-range ordering interacting with Al atoms in the α phase. The planar slip is more intense due to the presence of small, coherent, ordered Ti_3Al (α_2) particles [50,51]. The Ti-6242S alloy investigated in this work contains a high Al content of 6 wt%, so the dislocation substructure observed indeed revealed a planar configuration as shown in Fig. 7.

The CRSS ratios were computed using the statistical method explained in [14,24]. They are reported in Table 2 with results from other studies. The values of CRSS ratios differ from one study to another. Such variations can be attributed to the microstructure studied, its morphology, grain sizes, phase proportions, or even its texture. In this study, the evolution of the CRSS ratios was notably associated with the changing grain sizes and given for a specific texture (hot rolling) and specific phase proportions. Our basal<a> ratios were found to be around 1 and quite close to what can be found in the literature. As for the pyramidal<c+a> ratios, slightly higher values of 4.08–5.78 were achieved. Fig. 8 showcases the evolution of the CRSS ratios regarding grain size for two studied β fractions. According to our experimental observations, basal ratios were found to increase with coarser grains (thus prismatic systems would activate more than basal ones). Regarding pyramidal ratios, they inversely decreased with the increase in grain size. It is believed the main cause of such evolution was due to the frequent occurrence of prismatic slips with coarser grains rather than pyramidal slips themselves as we noticed that the relative number of such pyramidal slips was quite consistent in this study.

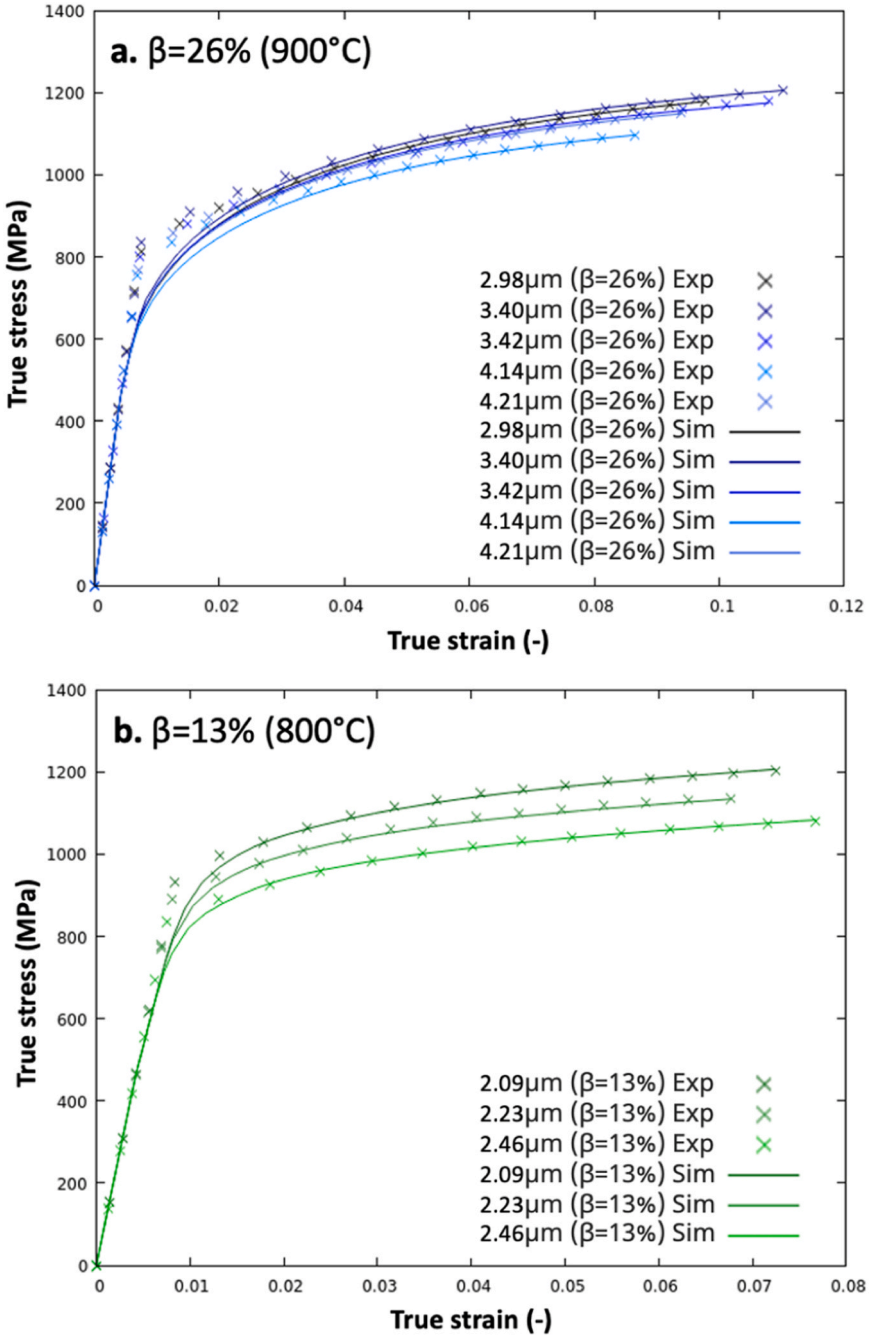

Fig. 9. Simulation results for tensile behaviors of equiaxed microstructures having **a.** 26% of β and **b.** 13% of β.

3.4. Numerical simulation

Using our experimental CRSS ratios to regulate some numerical parameters, we optimized our multiscale model to fit the experimental uniaxial tensile curves. Parameters for the pencil model (β phase) were calibrated for one grain size (d=3.42 μm) and then kept constant for the other grain sizes for consistency purposes. The values adopted for the material parameters are summarized in Table 3 for β = 26% and Table 4 for β = 13%. We can observe the evolution of the R_0 parameter (CRSS) which seems to increase for smaller grain sizes at both β fractions and especially for prismatic and pyramidal systems. A possible Hall-Petch linkage will be discussed afterward. On the other hand, the saturation stress Q depicts the difference between the maximum stress and the yield stress (CRSS) of the slip system and reflects a work hardening feature. It is worth noticing that thanks to our optimization binding choices regarding this parameter, the work hardening of each slip system is analogous to the macro work hardening observed in Fig. 4. Therefore, the simulations represent well the differences in work hardening when changing β fraction with Q parameters having higher values for the slip systems at 900 °C (β = 26%) than for the ones at 800 °C (β = 13%). Fig. 9 shows the simulation results of the fitted curves for tensile behaviors. Due to our optimization binding choices described in the optimization process Section 2.5.3, the yield zone was not perfectly fitted, especially for β = 26%. It could be possible the greater work hardening nature at β = 26% was a cause for the model to not perfectly fit the beginning of plasticity. Even so, the uniform region at higher stress could be accurately depicted.

Additionally in Fig. 10, we analyzed the evolution of the CRSS values regarding grain sizes and tried to look for a microscopic Hall-Petch relation that could help to better understand the deformation modes.

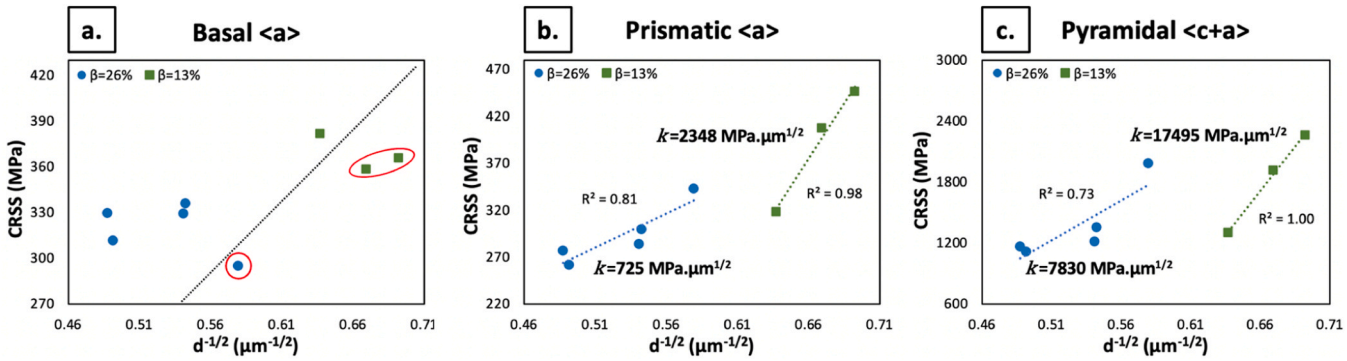

Fig. 10. Microscopic Hall-Petch relations for the CRSS values of **a.** basal<a> , **b.** prismatic<a> and **c.** pyramidal<c+a> slip systems.

Surprisingly we found prismatic<a> and pyramidal<c+a> slip systems were indeed related to grain size through Hall-Petch type equations. Also, we could see an interesting difference between the two proportion phases studied of $\beta = 26\%$ and $\beta = 13\%$. For prismatic<a> systems, the Hall-Petch constant of $\beta = 13\%$ was roughly 3x bigger than the one of $\beta = 26\%$. Picking up the thinking we had for global Hall-Petch constants at a macroscale, we understood the decrease of β fraction and thus of α-β boundaries allowed the harder α phase to contribute more and to increase the global Hall-Petch constant. With the same reasoning, we can suggest prismatic<a> systems are given more importance with higher α fractions (lower β fractions) which could explain such differences in Hall-Petch constants. The same observation was made for pyramidal<c+a> systems where the Hall-Petch constant was about 2x bigger for $\beta = 13\%$ than for $\beta = 26\%$.

Concerning basal<a> systems, we could not observe a Hall-Petch relation to link CRSS to grain sizes. We noticed the problematic data points came from small grain sizes where we measured basal ratios inferior to 1, meaning that basal<a> systems were now much more activated in fined-grained conditions. For such small grain sizes, the increase of the grain boundary density limits the mobility of the dislocations and the effects of dislocations pile-up at grain boundaries become more pronounced. These dislocations induce local stresses at boundary which can be accommodated by grain boundary sliding. Thus, grain boundary sliding is now another crucial mechanism to consider, especially with the need for HCP metals to accommodate incompatible deformation due to limited slip systems. Hémery et al. (2019) [52] found out grain boundary sliding was indeed an alternative deformation process mainly observed at high temperatures and/or in fined-grained materials. They also discovered that intragranular prismatic slipping was a trigger for grain boundary sliding in a Ti-6Al-4V alloy with bimodal microstructure at room temperature. Of the 972 total α nodules they analyzed, 875 showed apparent slipping and grain boundary sliding could be noticed for 6% of them. 80% of the observed grain boundary sliding was successfully associated with prismatic slip activity. While prismatic slipping was evidently involved in grain boundary sliding, the role of basal and pyramidal systems could not be clearly demonstrated. In the 20% of cases where grain boundary sliding was affiliated with basal and/or pyramidal slips, a possible prismatic slip activity underneath the sample surface could not be excluded.

On the other hand, J. Koike et al. (2003) [53] also studied the consequences of fined-grained microstructures on the deformation mechanisms at room temperature. While grain boundary sliding was also discussed, they additionally examined the effects of compatibility stresses in Mg alloys. Due to the elastic anisotropy of the crystals, compatibility stresses would arise from grain boundaries and activate the secondary intragranular slip systems. For Mg alloys and because of their higher c/a ratio (≈1.62), basal<a> systems are known to be the dominant slip systems. Therefore, the compatibility stresses principally activate prismatic<a> as secondary slipping in such fined-grained Mg alloys (their study dealt with grain sizes of 6.5 μm). H. Margolin and M. S. Stanescu (1975) [54] measured in their work that the length of the secondary slip lines adjacent to the grain boundaries is close to 10 μm regardless of a grain size that could vary from 49 to 94 μm. Hence, it supports the observations of J. Koike et al. (2003) [53] of the secondary intragranular slips being triggered by compatibility stresses coming from grain boundaries.

Coarse-grained alloys are known to promote the activation of the dominant slips more easily and exhibit microscopic yielding at lower stresses compared to fined-grained alloys. In fined-grained microstructures, the higher density of grain boundaries prevents a part of the dominant dislocations from slipping and increases local stresses at boundaries which activates secondary systems because of the compatibility stresses. Hence, we can understand grain size as a critical parameter in which the secondary intragranular slip will or will not be triggered by the influence of compatibility stress.

Conversely, the lower c/a ratio (≈1.59) of Ti alloys promotes prismatic<a> systems as the main slip systems. Now, if we apply the observations made for Mg alloys on our Ti-6242S alloy, we can speculate the basal<a> systems were activated as the secondary slips because of the compatibility stresses arising at very small grain sizes. The basal systems becoming more activated in such conditions, it could explain why the experimental CRSS basal ratios were decreasing with grain sizes and overtaking prismatic systems (ratio lower than 1).

Therefore, grain boundary sliding and compatibility stresses stand as additional mechanisms to take into account when studying deformation modes at very small grains. While clear links between grain size (Hall-Petch) and the activity of prismatic<a> and pyramidal<c+a> slip systems were exhibited in this study, the results regarding basal<a> slips in fined-grained conditions are believed to be strongly affected by these two additional mechanisms.

4. Conclusion

Ti-6242S samples with equiaxed ($\alpha + \beta$) microstructures were analyzed after uniaxial tensile deformation at room temperature. Increasing β fraction was impactful in improving the overall ductility and the work hardening while both grain size and β fraction played a part in controlling the material strength.

An extension of the Hall-Petch relation to dual-phase alloys was used to better understand the role of β fraction in the variations of the Hall-Petch constant. The computations allowed to emphasize the importance of phase proportions in the material strengthening due to grain size effect and also suggested a dependence on the mesoscopic Hall-Petch constants with β fraction.

Slip trace analysis was carried out for a qualitative understanding of the activation of the main deformation modes. CRSS ratios were computed for the basal<a> , prismatic<a> , and pyramidal<c+a> slip systems and were found to be related to grain size and β fraction. While prismatic systems were more easily activated for coarser grains, a larger amount of basal slips were observed at smaller grain sizes with CRSS

ratios lower than 1.

The experimental CRSS ratios also helped to identify the material parameters of a self-consistent multiscale model used to reproduce our tensile behaviors. The CRSS values of prismatic<a> and pyramidal<c+a> slip systems were successfully assessed and linked to grain sizes through Hall-Petch type equations. On the other hand, the relation between grain size or β fraction and the CRSS values of basal<a> systems was left unclear. The higher density of grain boundaries in fined-grained microstructures and the addition of the compatibility stresses and grain boundary sliding mechanisms were identified as possible causes.

CRediT authorship contribution statement

Velay Vincent: Writing – review & editing, Validation, Resources. **Dubray Clara:** Investigation. **Matsumoto Hiroaki:** Writing – review & editing, Validation, Supervision, Resources, Project administration, Methodology, Funding acquisition, Conceptualization. **Séchepée Irvin:** Writing – review & editing, Writing – original draft, Visualization, Validation, Software, Methodology, Investigation, Formal analysis, Conceptualization.

Declaration of Competing Interest

The authors declare that they have no known competing financial interests or personal relationships that could have appeared to influence the work reported in this paper.

Data availability

The authors do not have permission to share data.

Acknowledgments

This work was financially supported in part by a Grant-in-Aid for Scientific Research from the Light Metals Educational Foundation, Inc., 2022-C2-1., Japan.

References

[1] G. Lütjering, J.C. Williams, A. Gysler, Microstructure and Mechanical Properties of Titanium Alloys, in: J.C.M. Li (Ed.), Microstructure and Properties of Materials, World Scientific, Singapore, 2000, pp. 1–77, https://doi.org/10.1142/9789812793959_0001.

[2] M. Peters, J. Hemptenmacher, J. Kumpfert, C. Leyens, Structure and Properties of Titanium and Titanium Alloys, in: C. Leyens, M. Peters (Eds.), Titanium and Titanium Alloys: Fundamentals and Applications, Wiley-VCH, Weinheim, 2003, pp. 1–36, https://doi.org/10.1002/3527602119.ch1.

[3] I. Séchepée, P. Paulain, Y. Nagasaki, R. Tanaka, H. Matsumoto, V. Velay, Excellent balance of ultimate tensile strength and ductility in a Ti-6Al-2Sn-4Zr-2Mo-Si alloy having duplex α+α' microstructure: effect of microstructural factors from experimental study and machine learning, Mater. Trans. 64 (1) (2023) 111–120, https://doi.org/10.2320/matertrans.mt-mla2022009.

[4] P. Gao, M. Fu, M. Zhan, Z. Lei, Y. Li, Deformation behavior and microstructure evolution of titanium alloys with lamellar microstructure in hot working process: a review, J. Mater. Sci. Technol. 39 (2020) 56–73, https://doi.org/10.1016/j.jmst.2019.07.052.

[5] Z. Wang, L. Liu, L. Zhang, J. Sheng, D. Wu, M. Yuan, Effect of heat treatment on the microstructure and mechanical properties of high-strength Ti-6Al-4V–5Fe alloy, Mater. Trans. 60 (2) (2019) 269–276, https://doi.org/10.2320/matertrans.m2018267.

[6] Z. Fan, P. Tsakiropoulos, P.A. Smith, P. Miodownik, Extension of the Hall-Petch relation to two-ductile-phase alloys, Philos. Mag. A 67 (2) (1993) 515–531, https://doi.org/10.1080/01418619308207175.

[7] S. Graff, Micromechanical Modeling of the Deformation of HCP Metals, Thesis dissertation, Technische Universität Berlin, 2008.

[8] K. Kapoor, P. Ravi, R. Noraas, J.-S. Park, V. Venkatesh, M.D. Sangid, Modeling Ti-6Al-4V using crystal plasticity, calibrated with multi-scale experiments, to understand the effect of the orientation and morphology of the α and β phases on time dependent cyclic loading, J. Mech. Phys. Solids 146 (2021) 104192, https://doi.org/10.1016/j.jmps.2020.104192.

[9] M. Berveiller, A. Zaoui, An extension of the self-consistent scheme to plastically-flowing polycrystals, J. Mech. Phys. Solids 26 (1979) 325–344, https://doi.org/10.1016/0022-5096(78)90003-0.

[10] J.A. Moore, N.R. Barton, J. Florando, R. Mulay, M. Kumar, Crystal plasticity modeling of beta phase deformation in Ti-6Al-4V, Model. Simul. Mater. Sci. Eng. 25 (7) (2017) 075007, https://doi.org/10.1088/1361-651x/aa841c.

[11] S. Zaefferer, A study of active deformation systems in titanium alloys: dependence on alloy composition and correlation with deformation texture, Mater. Sci. Eng. A 344 (2003) 20–30, https://doi.org/10.1016/s0921-5093(02)00421-5.

[12] W. Tirry, F. Coghe, S. Bouvier, M. Gasperini, L. Rabet, D. Schryvers, A multi-scale characterization of deformation twins in Ti6Al4V sheet material deformed by simple shear, Mater. Sci. Eng. A 527 (2010) 4136–4145, https://doi.org/10.1016/j.msea.2010.03.039.

[13] B.R. Anne, Y. Okuyama, T. Morikawa, M. Tanaka, Activated slip systems in bimodal Ti-6Al-4V plastically deformed at low and moderately high temperatures, Mater. Sci. Eng. A 798 (2020) 140211, https://doi.org/10.1016/j.msea.2020.140211.

[14] F. Benmessaoud, M. Cheikh, V. Velay, V. Vidal, H. Matsumoto, Role of grain size and crystallographic texture on tensile behavior induced by sliding mechanism in Ti-6Al-4V alloy, Mater. Sci. Eng. A 774 (2020) 138835, https://doi.org/10.1016/j.msea.2019.138835.

[15] J. Gong, A.J. Wilkinson, Anisotropy in the plastic flow properties of single-crystal α titanium determined from micro-cantilever beams, Acta Mater. 57 (2009) 5693–5705, https://doi.org/10.1016/j.actamat.2009.07.064.

[16] F. Bridier, D.L. McDowell, P. Villechaise, J. Mendez, Crystal plasticity modeling of slip activity in Ti-6Al-4V under high cycle fatigue loading, Int. J. Plast. 25 (2009) 1066–1082, https://doi.org/10.1016/j.ijplas.2008.08.004.

[17] J.C. Williams, R.G. Baggerly, N.E. Paton, Deformation behavior of HCP Ti-Al alloy single crystals, Metall. Mater. Trans. A 33 (A) (2002) 837–850, https://doi.org/10.1007/s11661-002-0153-y.

[18] J. Galan-Lopez, S. Naghdy, P. Verleysen, L.A.I. Kestens, F. Coghe, L. Rabet, J. Degrieck, Mechanical behavior and texture prediction of Ti-6Al-4V based on elastic viscoplastic self-consistent modelling, IOP Conf. Ser.: Mater. Sci. Eng. 82 (2015) 012027, https://doi.org/10.1088/1757-899x/82/1/012027.

[19] J.R. Mayeur, D.L. McDowell, A three-dimensional crystal plasticity model for duplex Ti-6Al-4V, Int. J. Plast. 23 (2007) 1457–1485, https://doi.org/10.1016/j.ijplas.2006.11.006.

[20] N. Bertin, C.N. Tomé, I.J. Beyerlein, M.R. Barnett, L. Capolungo, On the strength of dislocation interactions and their effect on latent hardening in pure Magnesium, Int. J. Plast. 62 (2014) 72–92, https://doi.org/10.1016/j.ijplas.2014.06.010.

[21] R. Becker, Pencil glide formulation for polycrystal modelling, Scr. Metall. Mater. 32 (12) (1995) 2051–2054, https://doi.org/10.1016/0956-716x(95)00051-v.

[22] S. M'Guil, W. Wen, S. Ahzi, J.J. Gracio, Modeling of large plastic deformation behavior and anisotropy evolution in cold rolled bcc steels using the viscoplastic Φ-model-based grain-interaction, Mater. Sci. Eng. A 528 (2011) 5840–5853, https://doi.org/10.1016/j.msea.2011.03.110.

[23] L.T. Le, K. Ammar, S. Forest, Efficient simulation of single and poly-crystal plasticity based on the pencil glide mechanism, C. R. - Mec. 348 (10-11) (2020) 847–876, https://doi.org/10.5802/crmeca.44.

[24] H. Li, D.E. Mason, T.R. Bieler, C.J. Boehlert, M.A. Crimp, Methodology for estimating the critical resolved shear stress ratios of α-phase Ti using EBSD-based trace analysis, Acta Mater. 61 (2013) 7555–7567, https://doi.org/10.1016/j.actamat.2013.08.042.

[25] R. Zhang, Q. Zhao, Y. Zhao, D. Guo, Y. Du, Research progress on slip behavior of α-Ti under quasi-static loading: a review, Metals 12 (2022) 1571, https://doi.org/10.3390/met12101571.

[26] F. Bachmann, R. Hielscher, H. Schaeben, Texture analysis with MTEX – free and open source software toolbox, Solid State Phenom. 160 (2010) 63–68, https://doi.org/10.4028/www.scientific.net/ssp.160.63.

[27] L. Méric, P. Poubanne, G. Cailletaud, Single crystal modeling for structural calculations: Part 1 – Model presentation, J. Eng. Mater. Technol. 113 (1991) 162–170, https://doi.org/10.1115/1.2903374.

[28] J. Lemaitre, Background on Modeling, in: J. Lemaitre (Ed.), Handbook of Materials Behavior Models, Academic Press, San Diego, 2001, pp. 3–14, https://doi.org/10.1016/b978-012443341-0/50003-x.

[29] G. Cailletaud, Crystalline Viscoplasticity Applied to Single Crystals, in: J. Lemaitre (Ed.), Handbook of Materials Behavior Models, Academic Press, San Diego, 2001, pp. 303–317, https://doi.org/10.1016/b978-012443341-0/50034-x.

[30] Y. Yang, G. Vincze, C. Baudouin, H. Chalal, T. Balan, Strain-path dependent hardening models with rigorously identical predictions under monotonic loading, Mech. Res. Commun. (2021) 103615, https://doi.org/10.1016/j.mechrescom.2020.103615.

[31] W.-S. Lee, C.-F. Lin, Plastic deformation and fracture behaviour of Ti-6Al-4V alloy loaded with high strain rate under various temperatures, Mater. Sci. Eng. A 241 (1998) 48–59, https://doi.org/10.1016/s0921-5093(97)00471-1.

[32] T. Zhijun, Y. He, F. Xiaoguang (Eds.), Quasi-static tensile Behav. large-diameter thin-walled Ti-6Al-4V tubes Elev. Temp., Chin. J. Aeronaut. 29 (2) (2016) 542–553, https://doi.org/10.1016/j.cja.2015.08.004.

[33] G. Venkataramani, D. Deka, S. Ghosh, Crystal plasticity based FE model for understanding microstructural effects on creep and dwell fatigue in Ti-6242, J. Eng. Mater. Technol. 128 (2006) 356–365, https://doi.org/10.1115/1.2204942.

[34] T. Dick, G. Cailletaud, Fretting modelling with a crystal plasticity model of Ti6Al4V, Comput. Mater. Sci. 38 (2006) 113–125, https://doi.org/10.1016/j.commatsci.2006.01.015.

[35] V. Hasija, S. Ghosh, M.J. Mills, D.S. Joseph, Deformation and creep modeling in polycrystalline Ti-6Al alloys, Acta Mater. 51 (2003) 4533–4549, https://doi.org/10.1016/s1359-6454(03)00289-1.

[36] M.R. Bache, W.J. Evans, Impact of texture on mechanical properties in an advanced titanium alloy, Mater. Sci. Eng. A 319-321 (2001) 409–414, https://doi.org/10.1016/s0921-5093(00)02034-7.
[37] T. Mahender, M.R. Ananthan Padmanaban, I. Balasundar, T. Raghu, On the optimization of temperature and cooling rate to maximize strength and ductility of near α titanium alloy IMI 834, Mater. Sci. Eng. A 827 (2021) 142052, https://doi.org/10.1016/j.msea.2021.142052.
[38] H.R. Zhang, H.Z. Niu, M.C. Zang, H. Tan, D.L. Zhang, β-transformed domains enhanced tensile properties and the related deformation behavior of a near alpha titanium alloy, Mater. Sci. Eng. A (2021) 141902, https://doi.org/10.1016/j.msea.2021.141902.
[39] M.C. Zang, H.Z. Niu, S. Liu, H.R. Zhang, D.L. Zhang, Achieving high tensile strength-ductility synergy of a fully-lamellar structured near alpha titanium alloy at extra-low temperatures, J. Alloy. Compd. 923 (2022) 166363, https://doi.org/10.1016/j.jallcom.2022.166363.
[40] Y. Chong, G. Deng, S. Gao, J. Yi, A. Shibata, N. Tsuji, Yielding nature and Hall-Petch relationships in Ti-6Al-4V alloy with fully equiaxed and bimodal microstructures, Scr. Mater. 172 (2019) 77–82, https://doi.org/10.1016/j.scriptamat.2019.07.015.
[41] R.W. Armstrong, I. Codd, R.M. Douthwaite, N.J. Petch, The plastic deformation of polycrystalline aggregates, Philos. Mag. 7 (73) (1962) 45–58, https://doi.org/10.1080/14786436208201857.
[42] J.C.M. Li, Petch relation and grain boundary sources, Trans. Am. Inst. Metall. Eng. 227 (1) (1963) 239.
[43] M.F. Ashby, The deformation of plastically non-homogeneous materials, Philos. Mag. 21 (170) (1970) 399–424, https://doi.org/10.1080/14786437008238426.
[44] J. Luo, Z. Wang, On the physical meaning of the Hall-Petch constant, Adv. Mater. Res. 15 (2007) 643–648, https://doi.org/10.4028/www.scientific.net/amr.15-17.643.
[45] J.Y. Jung, J.K. Park, C.H. Chun, S.M. Her, Hall-Petch relation in two-phase TiAl alloys, Mater. Sci. Eng. A 220 (1-2) (1996) 185–190, https://doi.org/10.1016/s0921-5093(96)10446-9.
[46] J.A. Medina Perilla, J.Gil Sevillano, Two-dimensional sections of the yield locus of a Ti-6%Al-4%V alloy with a strong transverse-type crystallographic α-texture, Mater. Sci. Eng. A 201 (1995) 103–110, https://doi.org/10.1016/0921-5093(95)09780-5.
[47] T.R. Bieler, S.L. Semiatin, The effect of crystal orientation and boundary misorientation on tensile boundary cavitation during hot tension deformation of Ti-6Al-4V, in: K. Jata, E.W. Lee, W. Frazier, N.J. Kim (Eds.), Lightweight Alloys for Aerospace Application, Wiley, Hoboken, 2001, pp. 161–170, https://doi.org/10.1002/9781118787922.ch15.
[48] I.P. Jones, W.B. Hutchinson, Stress-state dependence of slip in titanium-6Al-4V and other H.C.P. metals, Acta Met. 29 (6) (1981) 951–968, https://doi.org/10.1016/0001-6160(81)90049-3.
[49] N.E. Paton, J.C. Williams, G.P. Rauscher, The deformation of α phase titanium, in: R.I. Jaffee, H.M. Burte (Eds.), Titanium Science Technology, Vol. 2, Plenum Press, New York, 1973, pp. 1049–1069.
[50] G. Lütjering, S. Weissmann, Mechanical properties of age-hardened titanium-aluminum alloys, Acta Met 18 (7) (1970) 785–795, https://doi.org/10.1016/0001-6160(70)90043-X.
[51] T. Neeraj, D.H. Hou, G.S. Daehn, M.J. Mills, Phenomenological and microstructural analysis of room temperature creep in titanium alloys, Acta Mater. 48 (6) (2000) 1225–1238, https://doi.org/10.1016/S1359-6454(99)00426-7.
[52] S. Hémery, C. Tromas, P. Villechaise, Slip-stimulated grain boundary sliding in Ti-6Al-4V at room temperature, Materialia 5 (2019) 100189, https://doi.org/10.1016/j.mtla.2018.100189.
[53] J. Koike, T. Kobayashi, T. Mukai, H. Watanabe, M. Suzuki, K. Maruyama, K. Higashi, The activity of non-basal slip systems and dynamic recovery at room temperature in fine-grained AZ31B magnesium alloys, Acta Mater. 51 (2003) 2055–2065, https://doi.org/10.1016/s1359-6454(03)00005-3.
[54] H. Margolin, M.S. Stanescu, Polycrystalline strengthening, Acta Met. 23 (12) (1975) 1411–1418, https://doi.org/10.1016/0001-6160(75)90150-9.